ACS APPLIED ELECTRONIC MATERIALS

pubs.acs.org/acsaelm

Article

Deep-UV Transparent Conducting Oxide La-Doped $SrSnO_3$ with a High Figure of Merit

Juhan Kim, Hwanhui Yun, Jihoon Seo, Jae Ha Kim, Jae Hoon Kim, K. Andre Mkhoyan, Bongju Kim,* and Kookrin Char*

Cite This: *ACS Appl. Electron. Mater.* 2022, 4, 3623−3631

Read Online

ACCESS | Metrics & More | Article Recommendations | Supporting Information

ABSTRACT: Perovskite stannate $SrSnO_3$ (SSO) is attracting attention as ultraviolet transparent conducting oxides (UV TCOs) due to its ultrawide band gap and high conductivity. Here, we investigate in detail the thickness-dependent electrical, structural, and optical properties of sequentially strain-relaxed La-doped $SrSnO_3$ (SLSO) epitaxial thin films. We find that the SLSO films grow as an orthorhombic *Pnma* phase with $a^-a^-c^+$ in the c^+ direction under the tensile strain. With the strain relaxation, as the films become thicker, vertical grain boundaries are created and the orthorhombic phase becomes reoriented to all three possible orientations. Simultaneously, the conductance starts to deviate from the linear behavior with increasing film thickness. Through the analysis of thickness fringes in optical transmittance, we found that a 120 nm thick nominally 4% La-doped $SrSnO_3$ film has a figure of merit ($\varphi_{TC} = 2.65 \times 10^{-3}\ \Omega^{-1}$) at $\lambda = 300$ nm in the deep-UV region, which is the highest value among the well-known candidates for UV TCOs reported to date.

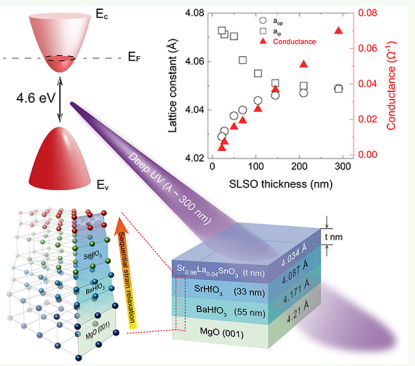

KEYWORDS: *ultraviolet transparent conducting oxides, figure of merit, La-doped $SrSnO_3$, ultrawide band gap semiconductors, thickness-dependent properties*

1. INTRODUCTION

The need for deep-ultraviolet transparent conducting oxides (DUV TCOs) has been growing steadily. Accordingly, the search for high conductance in ultrawide band gap (E_g > 4.0 eV) materials becomes important. DUV TCOs are most likely to be applied as transparent electrodes in ultraviolet light-emitting diodes (UV LEDs). In the last decade, UV LEDs are gradually emerging as a new UV source and replacing the traditional UV mercury lamps since they have a number of advantages, such as free of mercury, higher energy efficiency, longer lifetime, and fast operations.[1,2] This promising alternative can be employed in a wide range of applications such as decontamination of various food products,[3] disinfection of water,[4,5] sensing for biomolecules,[6] UV curing,[7] and UV phototherapy.[8] At the same time, UV detection and spectroscopy are becoming increasingly important for space and military applications.[9−11] However, a current roadblock toward such wide applications is that the light extraction and/or detection efficiency is still low in the deeper UV range due to absorption at the top contact layer of an LED or a detector.[12,13] Therefore, it is essential to develop transparent electrode materials that are highly conductive and transparent in the UV range. Al-doped ZnO (AZO)[14] and Sn-doped In_2O_3 (ITO)[15] are widely used as transparent electrodes for LEDs. However, they have an insufficient transparency in the deep-UV region (λ = 300 nm) due to their small band gap: E_g ~ 3.27 eV for AZO[16] and E_g ~ 3.6 eV for ITO.[17]

To date, two classes of materials have been proposed as UV transparent conducting oxide candidates. One is correlated metals, which have strong electron−electron interactions, such as $SrNbO_3$,[18,19] $CaVO_3$,[2020] and $SrVO_3$.[20,21] The other class is doped semiconductors with an ultrawide band gap such as Sn-doped β-Ga_2O_3 (E_g ~ 4.9 eV),[22] Sn-doped α-Ga_2O_3 (E_g ~ 5.3 eV),[23] and La-doped $SrSnO_3$ (E_g ~ 4.6 eV).[24,25] Among the materials corresponding to the former class, $CaVO_3$ and $SrVO_3$, perovskite vannadates, have excellent conductivity over 10^4 S cm^{-1}. This high conductivity comparable to ITO comes from the higher carrier density (n ~ 10^{22} cm^{-3}) with high effective mass due to the strong Coulomb interaction between electrons. However, their optical transmittance for energies above ~3.3 eV is suppressed and the transmittance is under 50% in the deep-UV region.[20,26] In the case of $SrNbO_3$, there is no direct measurement data yet for optical transmittance, although it has just been calculated to be over 80% from the absorption coefficient through the complex dielectric function obtained by spectroscopic ellipsometry.[18,19] Sn-doped α-Ga_2O_3 and Sn-doped β-Ga_2O_3 are candidates for UV TCOs

Received: May 3, 2022
Accepted: June 25, 2022
Published: July 11, 2022

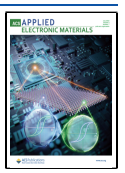

https://doi.org/10.1021/acsaelm.2c00581
ACS Appl. Electron. Mater. 2022, 4, 3623−3631

belonging to the latter class. However, they have poor transparency in the deep-UV range at the Sn-doping concentration required for the large conductance.[27,28] In the case of Sn-doped β-Ga_2O_3, the band gap greatly decreases from 4.9 eV for undoped to 4.1 eV at the optimum doping rate of 10%, resulting in decrease of transmittance from 60 to 5% at 300 nm.[27] A similar phenomenon is observed in Sn-doped α-Ga_2O_3; its optical transmittance reduces from 80% for 0.005% Sn doping to 50% at the optimum doping rate of 0.1%.[28] Another disadvantage is that they have a high electrical resistivity due to the low dopant solubility limit and degradation of crystallinity with increasing dopant concentration.[27,28]

Very recently, La-doped $SrSnO_3$ (SLSO) has emerged as one of the perovskite-structured alkaline stannates which have a potential for transparent conducting oxides due to their superior electrical conductivity and ultrawide band gap.[24] The conduction band of perovskite stannates originating mainly from the Sn-5s orbital leads to small electron effective mass and high electron mobility in spite of degenerate doping.[29] La-doped $BaSnO_3$ single crystals and epitaxial films are shown to have an outstanding electron mobility of 320 and 150 $cm^2\ V^{-1}\ s^{-1}$, respectively.[30,31] $SrSnO_3$ possesses a wider band gap ($E_g \sim 4.6$ eV) and smaller effective mass ($m_e \sim 0.23\ m_0$)[24] than $BaSnO_3$ ($E_g \sim 3.1$ eV, $m_e \sim 0.42\ m_0$).[32,33] In bulk powders, an orthorhombic phase (*Pnma*) is known to be the stable phase at room temperature[34] with lattice constants of $a_{ortho} = 5.703$ Å, $b_{ortho} = 5.709$ Å, and $c_{ortho} = 8.065$ Å (its pseudocubic lattice constant $a_{pc} = 4.034$ Å).[35] Trivalent ions such as La^{3+}, Ta^{3+}, Nd^{3+}, and Sm^{3+} were used as effective n-type dopants[36−46] by substituting for the Sr site without affecting the band structure.[47] Additionally, pentavalent ions such as Nb^{5+}, Sb^{5+}, and Pb^{5+} in place of Sn were studied as n-type dopants.[48−50] It is worth noting that the La dopant creates shallow donor levels in $SrSnO_3$, which indicates that extra electrons in La ions are easily activated.[47] The recently reported 3% La-doped $SrSnO_3$ (SLSO) film has the electron mobility as high as 56 $cm^2\ V^{-1}\ s^{-1}$ with the carrier density ($n \sim 3.26 \times 10^{20}\ cm^{-3}$), resulting in the highest conductivity ($\sigma \sim 3000$ S cm^{-1}) ever reported for $SrSnO_3$.[24] The solubility of La ions in SLSO films was reported to be enhanced through the postdeposition vacuum-annealing process.

In this paper, we report systematic studies on the thickness-dependent properties of highly conductive and DUV-transparent La-doped $SrSnO_3$ films grown on epitaxial $SrHfO_3$ and $BaHfO_3$ buffer layers on MgO (001) substrates, all DUV-transparent materials, by pulsed laser deposition (PLD) as illustrated in Figure 1. We used a sequential strain relaxation method using a $BaHfO_3$ perovskite buffer layer, which has an ultrawide band gap ($E_g \sim 6.1$ eV)[51] and a lattice constant ($a = 4.171$ Å),[52] which matches well with that of MgO ($a = 4.21$ Å).[53] $SrHfO_3$ was chosen as the second buffer layer because it is also an ultrawide band gap ($E_g \sim 6.1$ eV)[54] perovskite with a lattice constant ($a_{pc} = 4.087$ Å)[55] between those of $BaHfO_3$ and $SrSnO_3$ ($a_{pc} = 4.034$ Å).[35] The structural properties are examined by a high-resolution X-ray diffractometer (HRXRD) and scanning transmission electron microscope (STEM). We found that as the orthorhombic phase of SLSO films becomes thicker, they begin to change its direction and their conductance starts to deteriorate. The optical transmittance is investigated to maximize the figure of merit by analyzing the thickness fringes displayed by thin-film interference.

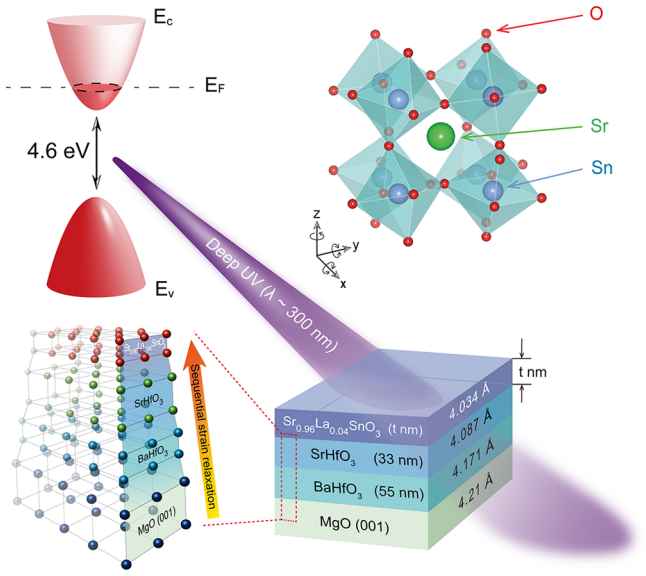

Figure 1. Tailoring of deep-UV transparent conducting oxide heterostructure. Schematics show sequential strain-relaxed and thickness-tuned nominally 4% La-doped $SrSnO_3$ films, which are highly conductive and transparent in the deep-UV range. $SrSnO_3$ (SSO) has an orthorhombic perovskite structure with the *Pnma space group* ($a^-a^-c^+$) *at room temperature with a pseudocubic lattice constant* ($a_{pc} = 4.034$ Å) *and a wide indirect band gap of 4.6 eV.*

2. RESULTS AND DISCUSSION

2.1. Doping Dependence of the Electrical Properties of 50 nm Thick SLSO Films. To investigate the effect of a nominal La-doping rate, we measured the electrical conductivity, the carrier density, and the Hall mobility of 50 nm thick $Sr_{1-x}La_xSnO_3$ thin films (x = 0.003, 0.005, 0.01, 0.02, 0.03, 0.04, 0.05) at room temperature. Figure 2a shows the current−voltage (I−V) data and the schematic for the Van der Pauw measurement used. Figure 2b−d shows the conductivity, Hall mobility, and carrier density, respectively. A significant increase in conductivity was observed at a 0.5% La-doping rate due to sharp increases in the carrier density (Figure 2d) and the Hall mobility (Figure 2c). As the nominal doping rate increases from 0.5 to 4%, the conductivity increases almost linearly with the nominal doping rate since there is little change in the Hall mobility, and the carrier density increases linearly. However, exceeding the nominal La-doping rate beyond 4%, the Hall mobility starts to decrease sharply, while the carrier density maintains the same trend. After a nominal 4% La-doping rate, scattering mechanisms by ionized and/or unionized La dopants seem dominant. Therefore, we found the optimum La-doping rate to be 4%; a 50 nm thick 4% SLSO film shows a high Hall mobility ($\mu = 44.14\ cm^2\ V^{-1}\ s^{-1}$) and large carrier density ($n_{3D} = 4.25 \times 10^{20}\ cm^{-3}$), and above all, the highest electrical conductivity ($\sigma \sim 3100$ S cm^{-1}) among the values of SLSO films reported to date. On the other hand, when the nominal La-doping rate drops from 0.5 to 0.3%, the Hall carrier density drops quickly from 4.01×10^{19} to $8.14 \times 10^{18}\ cm^{-3}$, and it was difficult to measure in 50 nm thick 0.25% SLSO films due to its high resistance. From this, we can infer that the deep acceptor density of our SLSO films is in the same range of the La^{3+} ion dopant density in 0.25% SLSO films ($n_{DA} \sim 3.81 \times 10^{19}\ cm^{-3}$).

2.2. Thickness Dependence of the Electrical Properties of 4% SLSO Films. To examine the electrical properties

https://doi.org/10.1021/acsaelm.2c00581
ACS Appl. Electron. Mater. 2022, 4, 3623−3631

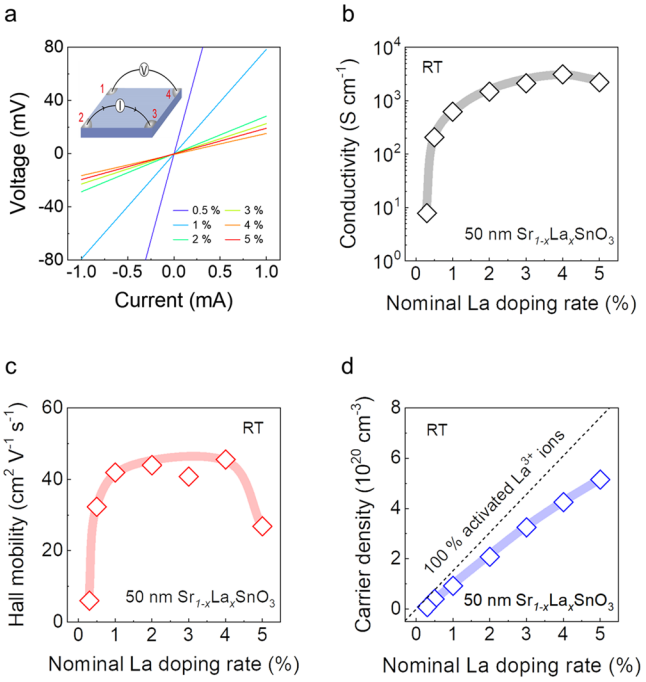

Figure 2. Doping dependence of electrical properties of 50 nm thick SLSO films grown on 33 nm thick SHO and 55 nm thick BHO buffers on the MgO (001) substrate at room temperature. (a) Voltage measured between 1 and 4 of the film by applying a current between 2 and 3 of the film. The inset is a schematic of Van der Pauw measurements. Indium was used as a contact. (b) Electrical conductivity, (c) Hall mobility, and (d) carrier density. A black thick dotted line represents the carrier density when La ions in the films are 100% activated.

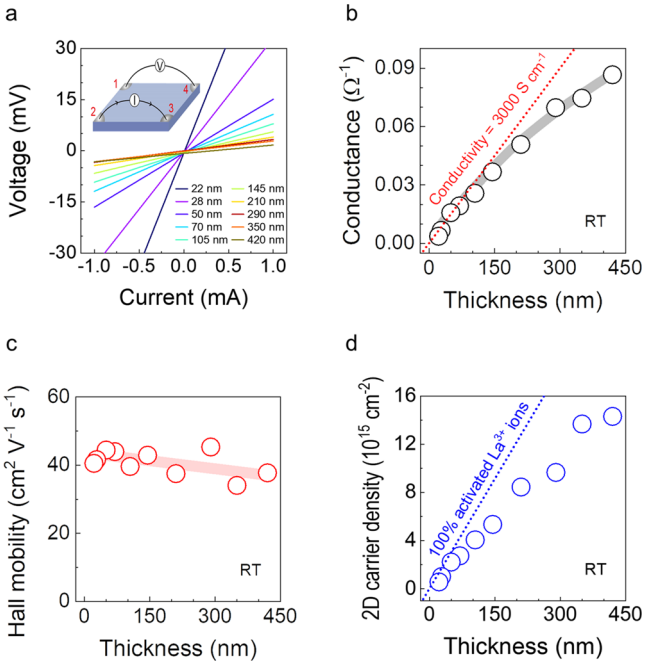

Figure 3. Thickness-dependent electrical properties of 4% SLSO films grown on 33 nm thick SHO and 55 nm thick BHO buffers on the MgO (001) substrate at room temperature. (a) Voltage measured between 1 and 4 of the film by applying a current between 2 and 3 of the film. (b) Conductance gradually deviates from the red dotted line representing the conductivity of 3000 S cm^{-1} with increasing film thickness. (c) Hall mobility slightly decreases as the film thickness increases. (d) Two-dimensional carrier density follows the blue dotted line representing the three-dimentional (3D) carrier density when La ions in the film are 100% activated.

depending on the thickness of 4% SLSO films, we fabricated t nm thick 4% SLSO films (t = 22, 28, 50, 70, 105, 145, 210, 290, 350, 420) grown on 33 nm thick $SrHfO_3$ and 55 nm thick $BaHfO_3$ buffer layers on the MgO (001) substrate. Figure 3a depicts the I−V data and a schematic for our Van der Pauw measurement. The conductance is not in a linear relationship with 4% SLSO film thickness, as illustrated in Figure 3b. Looking at the slope of the conductance up to 145 nm, the extracted conductivity is about 3000 S cm^{-1}. However, beyond the thickness of 145 nm, the conductance does not increase as expected and starts to deviate from the 3000 S cm^{-1} line. The Hall mobility in Figure 3c tends to decrease slightly with the increasing film thickness. The two-dimensional (2D) carrier density increases linearly with the film thickness, as illustrated in Figure 3d. As a result, the conductance, which is proportional to the product of mobility and 2D carrier density, deviates further from the trend when exceeding the thickness of 145 nm. It suggests that there exists a change in microstructure in films as the thickness increases, which tends to impede the current flow.

2.3. Structural Properties of 4% SLSO. To study the phenomenon discussed above in detail, we investigate the structural properties of t nm thick 4% SLSO films. Figure 4a,b shows the results of high-resolution X-ray θ−2θ scans and rocking curves of t nm thick 4% SLSO films (t = 22, 50, 105, 145, 290). In Figure 4a, the 2θ peak positions of the MgO (a_{op} = 4.217 Å) (001) substrate and the $BaHfO_3$ (a_{op} ∼ 4.184 Å) and $SrHfO_3$ (a_{op} ∼ 4.101 Å) buffer layers do not move, regardless of 4% SLSO thickness. The thickness fringes of $BaHfO_3$ around the (002) diffraction peak can be observed. From the spacing between the fringes, the $BaHfO_3$ thickness was calculated to be 53 nm, and it agrees with those measured by the stylus profiler and transmission electron microscopy (TEM). As the thickness of the 4% SLSO film increased, the 2θ peak position of 4% SLSO shifted to the left. It is seen clearly between t = 50 and 105 nm. Simultaneously, the symmetric peak shape of the 4% SLSO film becomes asymmetric beyond the thickness of 50 nm. Figure 4e−g shows the results of deconvoluting 50, 105, and 290 nm thick 4% SLSO asymmetric peaks using the Voigt functions. The 50 nm thick film peak is well fitted with only one Voigt function and its position is very close to the peak position of the 22 nm thick film in the Supporting Information (Figure S1a). However, in the case of the 105 nm and 290 nm thick films, the additional peak (peak 2) is necessary to fit the experimental data. The sums of the two peaks can be very well fitted to the experimental data (black circles). Therefore, either a new orientation or a new phase, corresponding to peak 2, starts to appear in the thickness range between 50 and 105 nm. The case of 145 nm thick film in the Supporting Information (Figure S1b) is the same as the case of 105 nm. It is highly likely that the tensile strain is relieved by creating a new orientation or a new phase as the 4% SLSO films become thicker. This is in contrast to the previously reported situation, where the compressive strain on $GdScO_3$ (110) substrates is relaxed as the SLSO film becomes thicker.[44,45] Figure 4c illustrates the rocking curves for 105 nm 4% SLSO, 33 nm $SrHfO_3$, 55 nm $BaHfO_3$ and the MgO (001) substrate. The MgO (001) single-crystal substrate has a sharp peak shape with

https://doi.org/10.1021/acsaelm.2c00581
ACS Appl. Electron. Mater. 2022, 4, 3623−3631

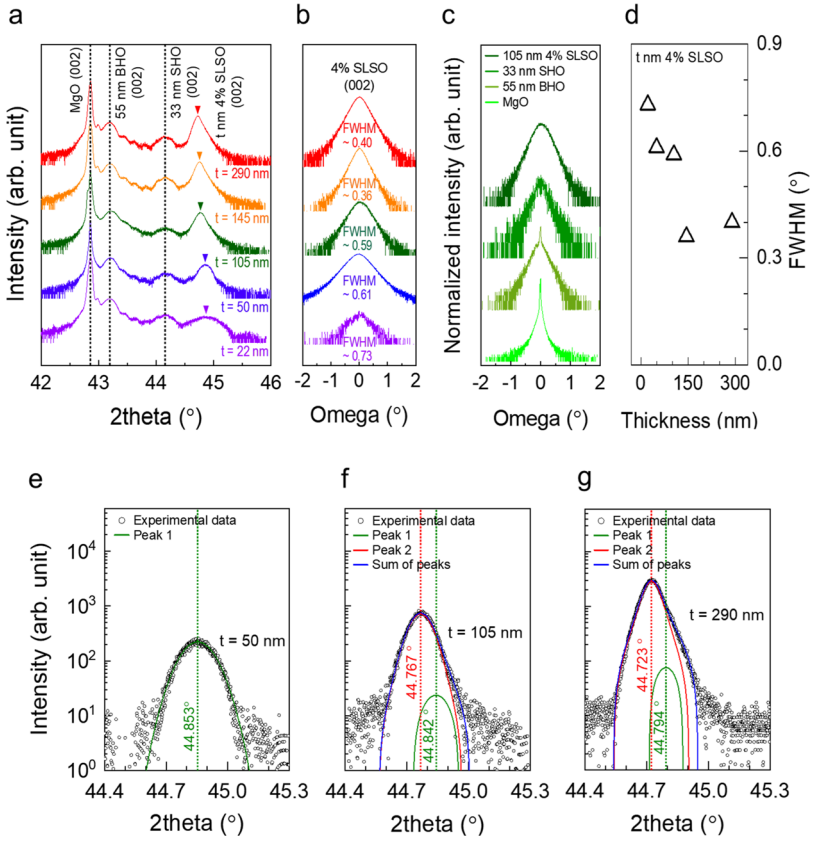

Figure 4. Thickness-dependent high-resolution X-ray diffraction. (a) θ–2θ scan and (b) rocking curves of t nm thick 4% SLSO films. (c) Rocking curves of 105 nm thick 4% SLSO, 33 nm thick SHO, and 55 nm thick BHO and MgO in order from the top. (d) FWHM for t nm thick 4% SLSO, 33 nm thick SHO, and 55 nm thick BHO as a function of t. (e–g) Results of the deconvolution of 2θ peaks using the Voigt functions for 50, 105, and 290 nm thick 4% SLSO films, respectively. (e) 2θ peak of 50 nm thick 4% SLSO is well fitted by only one Voigt function (green line) to the measured data (black circles). However, in the case of (f) 105 and (g) 290 nm thick 4% SLSO, the 2θ peaks are well fitted by two Voigt functions (green and red lines) to the measured data. Blue lines in panels (f, g) are the summation of peak 1 and peak 2.

full width at half-maximum (FWHM) of around 0.032. The rocking curve of 55 nm $BaHfO_3$ consists of two Gaussian functions: narrow and broad Gaussian functions, which suggests that 55 nm $BaHfO_3$ is partially relaxed on the MgO substrate. Typically, 33 nm $SrHfO_3$ and 105 nm 4% SLSO with an orthorhombic structure have wider rocking curves than cubic $BaHfO_3$ and the single-crystal MgO substrate. The full width at half-maximum (FWHM) values of the rocking curves of the 4% SLSO films gradually decrease with increasing the film thickness, as illustrated in Figure 4d.

To investigate the structural properties in detail, we measure the asymmetric reciprocal space mapping (RSM) for the (024) plane and (002) plane for t nm thick 4% SLSO, 33 nm thick $SrHfO_3$, and 55 nm thick $BaHfO_3$ and MgO. Figure 5a,b shows the reciprocal space mapping (RSM) results around the (024) plane for 22 and 290 nm thick 4% SLSO, respectively. MgO, $BaHfO_3$, $SrHfO_3$, and 4% SLSO peaks sequentially appear from the bottom. The RSM results for the (024) plane of 28, 50, 70, 105, 145, and 210 nm thick 4% SLSO films are shown in the Supporting Information (Figure S2). The schematic display of the four peaks can be shown in Figure 5a,b. The 290 nm thick 4% SLSO peak consists of a light and a dark green ellipse. In light of the 4% SLSO peak deconvolution results in Figure 4, we can interpret that the light green corresponds to peak 1, and the dark green corresponds to peak 2. The horizontal long black dotted lines are the value corresponding to the reciprocal space vector Q_z at each peak position. In line with the previous θ–2θ scan results, the peak positions of $BaHfO_3$, $SrHfO_3$, and MgO do not change, regardless of 4% SLSO thickness. Compared with the 22 and 290 nm thick 4% SLSO peaks, one can notice that their shapes and positions are changed. Even the 22 nm thick 4% SLSO does not grow coherently on the $SrHfO_3$ buffer layer from the fact that their reciprocal space vector Q_x is not the same. Figure 5c,d shows the reciprocal space mapping (RSM) around the (002) plane for 22 and 290 nm thick 4% SLSO films, respectively. One can observe the thickness fringes of a 55 nm $BaHfO_3$ buffer layer. The widths of the four peaks in Figure 5c in the reciprocal space vector Q_x direction seem constant. However, the width of 290 nm 4% SLSO peak in Figure 5d in the Q_x direction is definitely larger. Consequently, the (002) RSM results confirmed again that a new orientation or a new phase is formed as the 4% SLSO thickness increases. Figure 5e shows the in-plane (a_{ip}) and out-of-plane (a_{op}) lattice constants for 4% SLSO calculated from the RSM (024) data as a function of the 4% SLSO film thickness. As the film thickness increases, the tensile strain by the $SrHfO_3$ buffer gets relaxed and a noticeable drop in the in-plane lattice constant can be observed between 50 and 70 nm thickness. The in-plane and out-of-plane lattice constants eventually merge with each other as the films become thicker.

Since it is clear that the microstructure of the films changes as a function of the SLSO thickness, scanning transmission electron microscopy (STEM) experiments were conducted

https://doi.org/10.1021/acsaelm.2c00581
ACS Appl. Electron. Mater. 2022, 4, 3623–3631

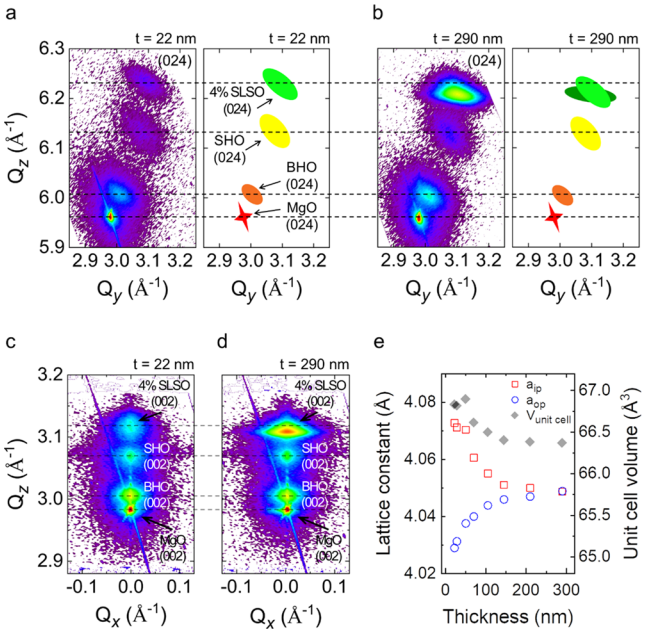

Figure 5. Thickness-dependent reciprocal space mapping (RSM). (a, b) RSM images for the (024) plane and the corresponding schematics of peak shape of 22 and 290 nm thick 4% SLSO films, respectively. (c, d) RSM images for the (002) plane of 22 and 290 nm thick 4% SLSO films, respectively. The horizontal black dotted lines represent the value of the reciprocal space vector (Q_z) corresponding to the four peaks in the RSM (024) and RSM (002) images for the 22 nm thick 4% SLSO film. (e) In-plane (a_{ip}), the out-of-plane lattice constants (a_{op}), and the unit cell volume ($V_{unit\ cell}$) of the 4% SLSO films calculated from the RSM (024) as a function of the film thickness.

(see the Supporting Information, Figures S3 and S5 for basic structural and compositional characterizations of $SrSnO_3$ films using STEM-energy-dispersive X-ray (EDX) analysis). In Figure 6a, a cross-sectional high-angle annular dark-field (HAADF)-STEM image of the 290 nm thick 4% SLSO film is presented, where the growth of columnar grains with the width of 10−50 nm is noted from the grain boundary contrasts. High-resolution bright-field (BF)-STEM images acquired from the top and bottom regions show distinct patterns (Figure 6b). At the bottom, only a lateral stripe pattern with two-unit-cell periodicity along the z-direction is seen, whereas three dissimilar patterns—lateral stripe, vertical stripe, and cross patterns—in different grains are observed in the top region. STEM images of a 22 nm thick SLSO film show only lateral patterns (see the Supporting Information, Figure S3c), implying the development of different crystal orientations in the $SrSnO_3$ grains with the film growth. Fast Fourier transforms (FFTs) obtained from the grains with the distinct patterns are shown in Figure 6c, where the appearance of spots corresponding to (022) (highlighted with the green circles), (002) (yellow circles), and (020) (violet circles) planes from the cross, lateral, and vertical patterns is witnessed.

At room temperature, $SrSnO_3$ exhibits an orthorhombic phase (space group of *Pnma*) with the SnO_6 octahedral rotation pattern of $a^-a^-c^+$ in the Glazer notation.[56] Figure 7 shows the atomic model of the *Pnma* phase $SrSnO_3$ projected in three Cartesian axes along the in-phase (c^+) (Figure 7a) and out-of-phase (a^-) (Figure 7b,c) octahedral rotation directions. Here, the projection direction is denoted as the x-axis, and the film growth direction is the z-axis. The projected image in the c^+ direction (Figure 7a) shows the in-phase octahedral rotation from corresponding O displacements; however, the image from the a^- direction (Figure 7b,c) does not since the rotations in the opposite (clockwise and anticlockwise) directions are overlapped. Atomic-resolution BF-STEM images were obtained to connect the atomic structure viewed in different orientations with the three types of grains. As presented in Figure 7, dark contrast appears at the atomic positions, which enables visualization of light O atoms and subtle atomic displacements in the structure. First, a BF-STEM image producing the cross pattern shows the O displacement corresponding to the octahedral rotation, suggesting that the projection direction of the STEM image is the c^+ direction, i.e., $c^+a^-a^-$. In the case of the stripe-patterned BF-STEM images, such O pattern is not discernable, but slight Sr displacements along the stripe lines are seen, which is the result of the atomic images projected in the a^- direction. A comparison between the atomic model and BF-STEM images reveals that the stripe pattern is generated from an alternating Sr displacement

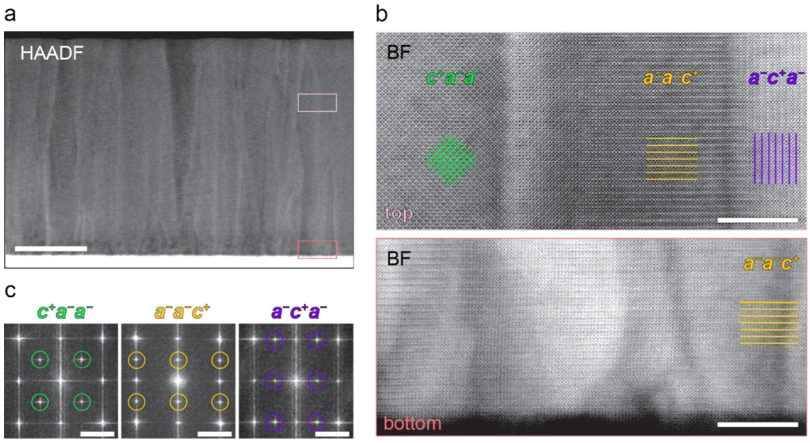

Figure 6. Atomic images of 4% SLSO films. (a) HAADF-STEM image of a 290 nm thick 4% SLSO film. The top and bottom regions in the film are indicated with pink and red rectangular boxes, respectively. The scale bar is 100 nm. (b) High-resolution BF-STEM images from top and bottom regions in the 4% SLSO film. Distinct patterns in different grains are highlighted. The scale bars are 10 nm. (c) FFTs obtained from the top region. Spots from $SrSnO_3$ grains with different orientations are circled with color codes: green ($c^+a^-a^-$), yellow ($a^-a^-c^+$), and violet ($a^-c^+a^-$). The scale bars are 0.2 $Å^{-1}$.

https://doi.org/10.1021/acsaelm.2c00581
ACS Appl. Electron. Mater. 2022, 4, 3623−3631

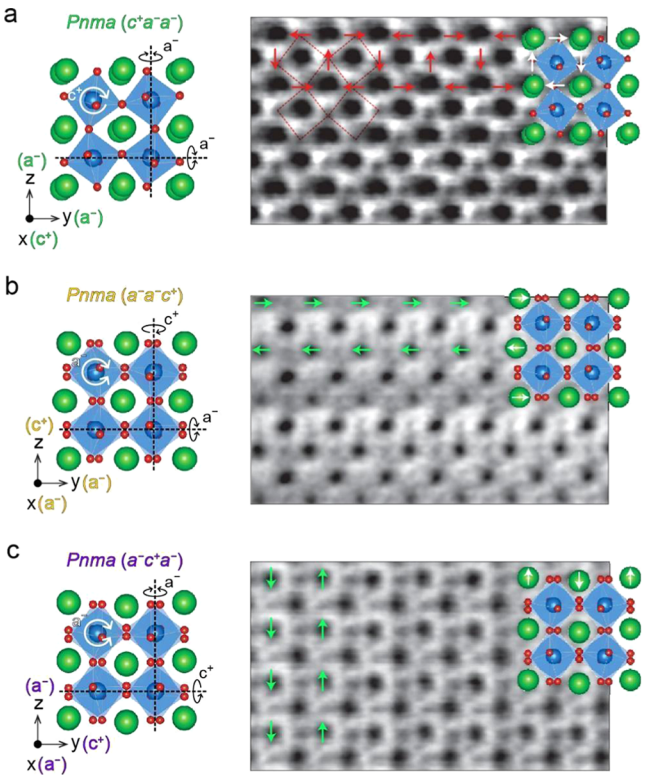

Figure 7. Atomic model and BF-STEM images of 4% SLSO. (a–c) Atomic model of the orthorhombic *Pnma* $SrSnO_3$ *structure viewed along the in-phase* (c^+) *and out-of-phase* (a^-) *octahedral rotation directions. Here, the x-direction is the viewing direction, and the z-direction is the film growth direction. Atomic-resolution BF-STEM images from grains with different orientations. Atomic models are overlaid. The O atomic positions showing the in-phase octahedral rotation are highlighted with red arrows, and the Sn atomic displacement directions are marked with green arrows.*

pattern that is perpendicular to the c^+ direction. Thus, in the case of grains displaying a lateral stripe pattern, the c^+ direction is along the *z*-axis (growth direction), i.e., $a^-a^-c^+$, while the vertical stripe pattern develops when the c^+ axis is the *y*-axis, i.e., $a^-c^+a^-$. The development and distribution of the reoriented grains were inspected from the Fourier filtered images using the unique spots from each orientation as presented in the Supporting Information (Figure S4a). The reoriented grains starting from ∼50 nm above the film–substrate interface are evidenced, which agrees with the lattice parameter change evidenced in the X-ray diffraction experiments. The BF-STEM image of the boundary between the initial and oriented grains exhibits a continuous but clearly distinct boundary between two regions (see the Supporting Information, Figure S4b).

STEM analysis concludes that the $SrSnO_3$ films initially grow along the c^+ direction under the tensile strain, and then, with the strain relaxation, grains are reoriented to all three possible orientations. Since the bulk lattice parameters of the *Pnma* phase are 4.035 and 4.033 Å along the a^- and c^+ directions, respectively,[40] the initial growth of $a^-a^-c^+$ alignment with larger lattice parameters being the in-plane axes can be stabilized with the imposed tensile strain. It should be noted that while recent studies have reported strain-driven phase transition of $SrSnO_3$ to the tetragonal *I*4/*mcm* phase with an octahedral rotation pattern of $a^0a^0c^-$,[40,45] XRD result from the films studied here shows significantly smaller (∼3%) out-of-plane lattice parameters compared to those of the tetragonal phase and, therefore, excludes the possibility of tetragonal phase formation.

2.4. Optical Properties of 4% SLSO Films. Optical transmittance spectra of *t* nm thick 4% SLSO films (*t* = 50, 70, 105, 145, 210, 290) are measured as a function of wavelength in Figure 8a. As the film thickness increases, the absorption

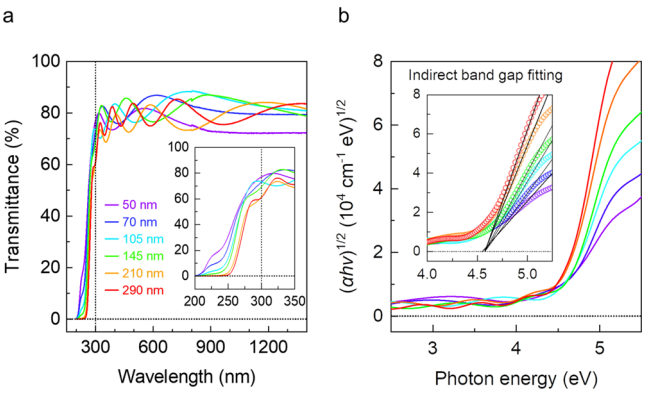

Figure 8. Thickness-dependent optical properties of 4% SLSO films. (a) Optical transmittance spectra vs wavelength of 4% SLSO films with various thicknesses. The inset shows a magnification of the optical transmission spectra in the UV region. A black dotted vertical line represents the wavelength of 300 nm. (b) Optical indirect band gap vs photon energy of 4% SLSO films with various thicknesses. The inset is the results of indirect band gap fitting for 4% SLSO films. At all thicknesses, the indirect band gap is about 4.6 eV.

becomes stronger and the number of fringes by thin-film interference increases. Analyzing the number of peaks and their positions, we believe that the interference fringes are caused by the reflections at the air/SLSO interface and the BHO/MgO interface. This is not surprising since the refractive indices of MgO, BHO, SHO, and SSO are 1.71 at 550 nm,[57] 2.5 at 300 nm,[58] 2.0 at 300 nm,[59] and 2.2 at 413 nm,[60] respectively. We obtained the highest optical transmittance in the DUV range (λ = 300 nm) of about 77.5% for a 120 nm thick 4% SLSO film, which is higher than the previously reported 73% transmittance at the wavelength of 300 nm in postdeposition vacuum-annealed 112 nm thick 3% SLSO.[24]

Figure 8b shows the $(\alpha h\nu)^{1/2}$–photon energy plot to estimate the indirect band gap of *t* nm thick 4% SLSO films, where α is the absorption coefficient, v is the frequency of the incident photon, and *h* is the Planck's constant, since $SrSnO_3$ is known to exhibit an indirect band gap.[61,62] The indirect band gap can be estimated by extrapolating the straight-line portion of the plot to the energy axis, illustrated in the inset of Figure 8b. Independent of the film thickness, the indirect band gap of *t* nm thick 4% SLSO is around 4.6 eV, which is similar to the previously reported value of 3% SLSO films estimated by assuming a direct band gap.[24] Our estimation for the direct band gap by plotting $(\alpha h\nu)^2$ vs photon energy is shown in Figure S6, which suggests that the direct band gap is about 4.9 eV.

Finally, we can calculate the figure of merit for transparent conductors[63] ($\varphi_{TC} = T^{10}/R_s$, where *T* is the transmission and R_s is the sheet resistance) at a wavelength of 300 nm, as shown in the Supporting Information (Table S1), and obtain φ_{TC} = 2.65 × 10^{-3} Ω^{-1} for 120 nm thick 4% SLSO, which is the highest value reported to date, among the candidates of deep-UV transparent conducting oxides such as Sn-doped β-Ga_2O_3

https://doi.org/10.1021/acsaelm.2c00581
ACS Appl. Electron. Mater. 2022, 4, 3623–3631

(φ_{TC} = 7.8 × 10^{-7} Ω^{-1})[22] and 3% La-doped $SrSnO_3$ (φ_{TC} = 1.45 × 10^{-3} Ω^{-1}).[24]

3. CONCLUSIONS

In conclusion, we have fabricated thickness-tuned 4% SLSO films grown on 33 nm $SrHfO_3$ and 55 nm $BaHfO_3$ buffers on the MgO (001) substrate by employing a sequential strain relaxation method. We have found that excellent conducting properties were obtained in 50 nm thick nominally 4% La-doped films with their high conductivity ($\sigma \sim 3100$ S cm^{-1}), large carrier density (n = 4.25 × 10^{20} cm^{-3}), and high Hall mobility (μ = 44.14 cm^2 V^{-1} s^{-1}). As the films become thicker, we found that the tensile strain exerted by a $SrHfO_3$ buffer layer is relaxed by forming grains in all three directions of the orthorhombic phase. At the same time, the conductance starts to deviate from the linear relationship with the film thickness due to the vertical grain boundaries that impede the transport of electrons. Via thickness tuning for the optical transmittance at a wavelength of 300 nm, a 120 nm 4% SLSO film was found to show the highest figure of merit calculated from the sheet resistance and transmittance. We demonstrate the great potential of 4% SLSO films for the next-generation deep-UV (λ = 300 nm) transparent conducting oxide (DUV TCO).

4. EXPERIMENTAL SECTION

4.1. Thin-Film Growth. All La-doped $SrSnO_3$ (SLSO) epitaxial thin films grown on 33 nm $SrHfO_3$ and 55 nm $BaHfO_3$ buffers on the MgO (001) single-crystal substrate by the PLD method (KrF excimer laser, λ = 248 nm, coherent). Two side-polished MgO (001) substrates (5 mm × 5 mm × 0.5 mm) were provided by MTI Korea. All targets of $BaHfO_3$, $SrHfO_3$, $SrSnO_3$, and 0.5, 1, 4, 8% La-doped $SrSnO_3$ were provided by Toshima manufacturing Co., Japan. First, a 55 nm $BaHfO_3$ buffer layer is grown on the MgO (001) substrate by PLD (energy influence = 1.44 J cm^{-2} and repetition rate = 10 Hz). The substrate temperature and oxygen partial pressure in the chamber were kept at 750 °C and 100 mTorr, respectively. The distance between the target and substrate is 51 mm. Second, the 33 nm $SrHfO_3$ buffer layer is grown on the 55 nm $BaHfO_3$ buffer layer by PLD (energy influence = 1.44 J cm^{-2} and repetition rate = 10 Hz). The substrate temperature and oxygen partial pressure in the chamber were kept at 750 °C and 100 mTorr, respectively. The distance between the target and substrate is 45 mm. Finally, SLSO is grown by PLD (energy influence = 1.55 J cm^{-2} and repetition rate = 4 Hz). The substrate temperature and oxygen partial pressure in the chamber were kept at 750 °C and 150 mTorr, respectively. The distance between the target and substrate is 55.5 mm. After deposition, the SLSO films were cooled in vacuum to 400 °C and in 600 Torr oxygen thereafter.

4.2. Structural Property Measurement. The structural properties of the SLSO films were analyzed by θ–2θ scan, rocking curves, and reciprocal space mapping (RSM). θ–2θ scan and rocking curves were conducted using a high-resolution X-ray diffractometer (D8 Discover, Bruker) at IBS Center for Correlated Electron Systems, Seoul National University. The reciprocal space mapping (RSM) is performed using SmartLab with a Cu Kα_1 source (λ = 1.5406 Å; Rigaku, Japan) at room temperature. An X-ray CBO system, a Ge (220) 2-bounce monochromator, and a one-dimensional semiconductor array detector (hybrid photon counting detector; HyPix-3000) were used for high-resolution crystalline qualities. A scanning transmission electron microscopy (STEM) experiment was conducted using a FEI Titan G2 60-300 (S)TEM equipped with a CEOS DCOR probe corrector, a Schottky extreme field emission gun, and a super-X energy dispersive X-ray (EDX) spectrometer. The STEM was operated at 200 keV with a beam current of ~30 pA, and the probe convergence angle was 25.5 mrad. High-angle annular dark-field (HAADF)-STEM images were acquired with the annular dark-field (ADF) detector inner angle of 93 mrad, and bright-field (BF)-STEM images were acquired with the BF detector outer angle of 19 mrad.

4.3. Electrical Property Measurement. The electrical properties of SLSO films were measured using a Keithley 4200 semiconductor characterization system. Indium was used as the contact. The Van der Pauw method was used in a 4-point geometry for determining the sheet resistance of the films. The Hall carrier density and mobility were determined by applying the magnetic field perpendicular to the films while measuring the change in resistance.

4.4. Optical Property Measurement. The optical transmittance of SLSO films was measured by a grating spectrometer (Cary 5000, Bruker) over 200–2000 nm (0.6–6.2 eV). The spectrometer has a QI lamp light source for 2000–350 nm and a deuterium UV lamp light source for below 350 nm. Samples are mounted on a holder with a 3 mm diameter hole. Absorbance is calculated as the minus logarithm of the transmittance, and the absorption coefficient α is calculated by accounting for the sample thickness. We removed the absorption of the substrate and two buffers by measuring their optical absorption separately and subtracting it from the absorbance. From the optical absorption measurement, we plotted the Tauc's plot of $(\alpha h\nu)^{1/2}$ vs photon energy, where α denotes the absorption coefficient.

■ ASSOCIATED CONTENT

Supporting Information

The Supporting Information is available free of charge at https://pubs.acs.org/doi/10.1021/acsaelm.2c00581.

Deconvolution of 2θ peaks; thickness-dependent reciprocal space mapping (RSM); HADDF- and BF-STEM images; EDX elemental maps; FFT filtered images, and thickness-dependent figure of merit (PDF)

■ AUTHOR INFORMATION

Corresponding Authors

Bongju Kim − *Institute of Applied Physics, Department of Physics and Astronomy, Seoul National University, Seoul 08826, Republic of Korea*; Email: bongju@snu.ac.kr

Kookrin Char − *Institute of Applied Physics, Department of Physics and Astronomy, Seoul National University, Seoul 08826, Republic of Korea*; orcid.org/0000-0001-6060-5448; Email: kchar@snu.ac.kr

Authors

Juhan Kim − *Institute of Applied Physics, Department of Physics and Astronomy, Seoul National University, Seoul 08826, Republic of Korea*

Hwanhui Yun − *Department of Chemical Engineering and Material Science, University of Minnesota, Minneapolis, Minnesota 55455, United States*

Jihoon Seo − *Institute of Applied Physics, Department of Physics and Astronomy, Seoul National University, Seoul 08826, Republic of Korea*

Jae Ha Kim − *Department of Physics, Yonsei University, Seoul 03722, Republic of Korea*

Jae Hoon Kim − *Department of Physics, Yonsei University, Seoul 03722, Republic of Korea*; orcid.org/0000-0002-7840-3630

K. Andre Mkhoyan − *Department of Chemical Engineering and Material Science, University of Minnesota, Minneapolis, Minnesota 55455, United States*; orcid.org/0000-0003-3568-5452

Complete contact information is available at: https://pubs.acs.org/10.1021/acsaelm.2c00581

https://doi.org/10.1021/acsaelm.2c00581
ACS Appl. Electron. Mater. 2022, 4, 3623–3631

Notes

The authors declare no competing financial interest.

■ ACKNOWLEDGMENTS

A part of this study has been performed using facilities at the IBS Center for Correlated Electron Systems, Seoul National University. The electron microscopy effort (H.Y. and K.A.M.) was supported by the NSF through the MRSEC (DMR-2011401). Parts of this work were carried out in the Characterization Facility, University of Minnesota, which receives partial support from the NSF through the MRSEC program. This work at Yonsei University was supported by the National Research Foundation (NRF) grants funded by the Korean government (MSIT; grant 2021R1A2C3004989) and the SRC program (vdWMRC; grant 2017R1A5A1014862).

■ REFERENCES

(1) Muramoto, Y.; Kimura, M.; Nouda, S. Development and future of ultraviolet light-emitting diodes: UV-LED will replace the UV lamp. *Semicond. Sci. Technol.* **2014**, *29*, No. 084004.
(2) Bettles, T.; Schujman, S.; Smart, J. A.; Liu, W.; Schowalter, L. UV Light Emitting Diodes - Their Applications and Benefits. *Int. Ultraviolet Assoc. News* **2007**, *9*, 11−15.
(3) Kebbi, Y.; Muhammad, A. I.; Sant'Ana, A. S.; do Prado-Silva, L.; Liu, D.; Ding, T. Recent advances on the application of UV-LED technology for microbial inactivation: Progress and mechanism. *Compr. Rev. Food Sci. Food Saf.* **2020**, *19*, 3501−3527.
(4) Song, K.; Mohseni, M.; Taghipour, F. Application of ultraviolet light-emitting diodes (UV-LEDs) for water disinfection: A review. *Water Res.* **2016**, *94*, 341−349.
(5) Würtele, M.; Kolbe, T.; Lipsz, M.; Kulberg, A.; Weyers, M.; Kneissl, M.; Jekel, M. Application of GaN-based ultraviolet-C light emitting diodes - UV LEDs - for water disinfection. *Water Res.* **2011**, *45*, 1481−1489.
(6) Kumamoto, Y.; Taguchi, A.; Kawata, S. Deep-Ultraviolet Biomolecular Imaging and Analysis. *Adv. Opt. Mater.* **2019**, *7*, No. 1801099.
(7) Sangermano, M.; Razza, N.; Crivello, J. V. Cationic UV-Curing: Technology and Applications. *Macromol. Mater. Eng.* **2014**, *299*, 775−793.
(8) Mendes, R. B.; Alpalhão, M.; Filipe, P. UVB phototherapy in the treatment of vitiligo: State of the art and clinical perspectives. *Photodermatol., Photoimmunol. Photomed.* **2022**, *38*, 215−223.
(9) Balducci, A.; Bruzzi, M.; De Sio, A.; Donato, M. G.; Faggio, G.; Marinelli, M.; Messina, G.; Milani, E.; Morgada, M. E.; Pace, E.; Pucella, G.; Santangelo, S.; Scoccia, M.; Scuderi, S.; Tucciarone, A.; Verona-Rinati, G. Diamond-based photoconductors for deep UV detection. *Nucl. Instrum. Methods Phys. Res., Sect. A* **2006**, *567*, 188−191.
(10) Razeghi, M.; Rogalski, A. Semiconductor ultraviolet detectors. *J. Appl. Phys.* **1996**, *79*, 7433−7473.
(11) Neele, F. P.; Schleijpen, J. In *Electro-Optical Missile Plume Detection*, SPIE Proceedings, 2003; pp 270−280.
(12) Shatalov, M.; Sun, W.; Lunev, A.; Hu, X.; Dobrinsky, A.; Bilenko, Y.; Yang, J.; Shur, M.; Gaska, R.; Moe, C.; Garrett, G.; Wraback, M. AlGaN Deep-Ultraviolet Light-Emitting Diodes with External Quantum Efficiency above 10%. *Appl. Phys. Express* **2012**, *5*, No. 082101.
(13) Takano, T.; Mino, T.; Sakai, J.; Noguchi, N.; Tsubaki, K.; Hirayama, H. Deep-ultraviolet light-emitting diodes with external quantum efficiency higher than 20% at 275 nm achieved by improving light-extraction efficiency. *Appl. Phys. Express* **2017**, *10*, No. 031002.
(14) Agura, H.; Suzuki, A.; Matsushita, T.; Aoki, T.; Okuda, M. Low resistivity transparent conducting Al-doped ZnO films prepared by pulsed laser deposition. *Thin Solid Films* **2003**, *445*, 263−267.
(15) Granqvist, C. G.; Hultåker, A. Transparent and conducting ITO films: new developments and applications. *Thin Solid Films* **2002**, *411*, 1−5.
(16) Banerjee, P.; Lee, W.-J.; Bae, K.-R.; Lee, S. B.; Rubloff, G. W. Structural, electrical, and optical properties of atomic layer deposition Al-doped ZnO films. *J. Appl. Phys.* **2010**, *108*, No. 043504.
(17) Thirumoorthi, M.; Prakash, J. T. J. Structure, optical and electrical properties of indium tin oxide ultra thin films prepared by jet nebulizer spray pyrolysis technique. *J. Asian Ceram. Soc.* **2016**, *4*, 124−132.
(18) Roth, J.; Paul, A.; Goldner, N.; Pogrebnyakov, A.; Agueda, K.; Birol, T.; Alem, N.; Engel-Herbert, R. Sputtered Sr_xNbO_3 as a UV-Transparent Conducting Film. *ACS Appl. Mater. Interfaces* **2020**, *12*, 30520−30529.
(19) Park, Y.; Roth, J.; Oka, D.; Hirose, Y.; Hasegawa, T.; Paul, A.; Pogrebnyakov, A.; Gopalan, V.; Birol, T.; Engel-Herbert, R. $SrNbO_3$ as a transparent conductor in the visible and ultraviolet spectra. *Commun. Phys.* **2020**, *3*, No. 102.
(20) Zhang, L.; Zhou, Y.; Guo, L.; Zhao, W.; Barnes, A.; Zhang, H. T.; Eaton, C.; Zheng, Y.; Brahlek, M.; Haneef, H. F.; Podraza, N. J.; Chan, M. H.; Gopalan, V.; Rabe, K. M.; Engel-Herbert, R. Correlated metals as transparent conductors. *Nat. Mater.* **2016**, *15*, 204−210.
(21) He, H.; Yang, Z.; Xu, Y.; Smith, A. T.; Yang, G.; Sun, L. Perovskite oxides as transparent semiconductors: a review. *Nano Convergence* **2020**, *7*, No. 32.
(22) Orita, M.; Ohta, H.; Hirano, M.; Hosono, H. Deep-ultraviolet transparent conductive β-Ga_2O_3 thin films. *Appl. Phys. Lett.* **2000**, *77*, 4166−4168.
(23) Shinohara, D.; Fujita, S. Heteroepitaxy of Corundum-Structured α-Ga_2O_3 Thin Films on α-Al_2O_3 Substrates by Ultrasonic Mist Chemical Vapor Deposition. *Jpn. J. Appl. Phys.* **2008**, *47*, 7311−7313.
(24) Wei, M.; Sanchela, A. V.; Feng, B.; Ikuhara, Y.; Cho, H. J.; Ohta, H. High electrical conducting deep-ultraviolet-transparent oxide semiconductor La-doped $SrSnO_3$ exceeding ~3000 S cm^{-1}. *Appl. Phys. Lett.* **2020**, *116*, No. 022103.
(25) Wei, M.; Cho, H. J.; Ohta, H. Tuning of the Optoelectronic Properties for Transparent Oxide Semiconductor $ASnO_3$ by Modulating the Size of A-Ions. *ACS Appl. Electron. Mater.* **2020**, *2*, 3971−3976.
(26) Jung, D. H.; So, H. S.; Lee, H. Structural and electrical properties of transparent conductor $SrVO_3$ thin films grown using radio frequency sputtering deposition. *J. Vac. Sci. Technol. A* **2019**, *37*, No. 021507.
(27) Mi, W.; Du, X.; Luan, C.; Xiao, H.; Ma, J. Electrical and optical characterizations of β-Ga_2O_3: Sn films deposited on MgO (110) substrate by MOCVD. *RSC Adv.* **2014**, *4*, 30579−30583.
(28) Chikoidze, E.; von Bardeleben, H. J.; Akaiwa, K.; Shigematsu, E.; Kaneko, K.; Fujita, S.; Dumont, Y. Electrical, optical, and magnetic properties of Sn doped α-Ga_2O_3 thin films. *J. Appl. Phys.* **2016**, *120*, No. 025109.
(29) Mizoguchi, H.; Eng, H. W.; Woodward, P. M. Probing the electronic structures of ternary perovskite and pyrochlore oxides containing Sn^{4+} or Sb^{5+}. *Inorg. Chem.* **2004**, *43*, 1667−1680.
(30) Kim, H. J.; Kim, U.; Kim, H. M.; Kim, T. H.; Mun, H. S.; Jeon, B.-G.; Hong, K. T.; Lee, W.-J.; Ju, C.; Kim, K. H.; Char, K. High Mobility in a Stable Transparent Perovskite Oxide. *Appl. Phys. Express* **2012**, *5*, No. 061102.
(31) Raghavan, S.; Schumann, T.; Kim, H.; Zhang, J. Y.; Cain, T. A.; Stemmer, S. High-mobility $BaSnO_3$ grown by oxide molecular beam epitaxy. *APL Mater.* **2016**, *4*, No. 016106.
(32) Shin, J.; Lim, J.; Ha, T.; Kim, Y. M.; Park, C.; Yu, J.; Kim, J. H.; Char, K. Band gap and mobility of epitaxial perovskite $BaSn_{1-x}Hf_xO_3$ thin films. *Phys. Rev. Mater.* **2018**, *2*, No. 021601.
(33) Kim, U.; Park, C.; Ha, T.; Kim, R.; Mun, H. S.; Kim, H. M.; Kim, H. J.; Kim, T. H.; Kim, N.; Yu, J.; Kim, K. H.; Kim, J. H.; Char, K. Dopant-site-dependent scattering by dislocations in epitaxial films of perovskite semiconductor $BaSnO_3$. *APL Mater.* **2014**, *2*, No. 056107.

https://doi.org/10.1021/acsaelm.2c00581
ACS Appl. Electron. Mater. 2022, 4, 3623−3631

(34) Glerup, M.; Knight, K. S.; Poulsen, F. W. High temperature structural phase transitions in $SrSnO_3$ perovskite. *Mater. Res. Bull.* **2005**, *40*, 507−520.
(35) Green, M. A.; Prassides, K.; Day, P.; Neumann, D. A. Structure of the n = 2 and n = ∞ member of the Ruddlesden-Popper series, $Sr_{n+1}Sn_nO_{3n+1}$. *Int. J. Inorg. Mater.* **2000**, *2*, 35−41.
(36) Wang, H.; Jiao, X.; Liu, Q.; Xuan, X.; Chen, F.; Wu, W. Transparent and conductive oxide films of the perovskite $La_xSr_{1-x}SnO_3$ ($x \leqslant 0.15$): epitaxial growth and application for transparent heterostructures. *J. Phys. D: Appl. Phys.* **2010**, *43*, No. 035403.
(37) Liu, Q.; Dai, J.; Zhang, X.; Zhu, G.; Liu, Z.; Ding, G. Perovskite-type transparent and conductive oxide films: Sb- and Nd-doped $SrSnO_3$. *Thin Solid Films* **2011**, *519*, 6059−6063.
(38) Baba, E.; Kan, D.; Yamada, Y.; Haruta, M.; Kurata, H.; Kanemitsu, Y.; Shimakawa, Y. Optical and transport properties of transparent conducting La-doped $SrSnO_3$ thin films. *J. Phys. D: Appl. Phys.* **2015**, *48*, No. 455106.
(39) Liu, Q.; Jin, F.; Gao, G.; Wang, W. Ta doped $SrSnO_3$ epitaxial films as transparent conductive oxide. *J. Alloys Compd.* **2017**, *717*, 62−68.
(40) Wang, T.; Prakash, A.; Dong, Y.; Truttmann, T.; Bucsek, A.; James, R.; Fong, D. D.; Kim, J. W.; Ryan, P. J.; Zhou, H.; Birol, T.; Jalan, B. Engineering $SrSnO_3$ Phases and Electron Mobility at Room Temperature Using Epitaxial Strain. *ACS Appl. Mater. Interfaces* **2018**, *10*, 43802−43808.
(41) Truttmann, T.; Prakash, A.; Yue, J.; Mates, T. E.; Jalan, B. Dopant solubility and charge compensation in La-doped $SrSnO_3$ films. *Appl. Phys. Lett.* **2019**, *115*, No. 152103.
(42) Kumar, Y.; Kumar, R.; Asokan, K.; Meena, R.; Choudhary, R. J.; Singh, A. P. Transport properties of perovskite-based stannate thin films of La-doped $SrSnO_3$. *Superlattices Microstruct.* **2021**, *158*, No. 107028.
(43) Kumar, Y.; Kumar, R.; Choudhary, R. J.; Thakur, A.; Singh, A. P. Reduction in the tilting of oxygen octahedron and its effect on bandgap with La doping in $SrSnO_3$. *Ceram. Int.* **2020**, *46*, 17569−17576.
(44) Prakash, A.; Wang, T.; Bucsek, A.; Truttmann, T. K.; Fali, A.; Cotrufo, M.; Yun, H.; Kim, J. W.; Ryan, P. J.; Mkhoyan, K. A.; Alu, A.; Abate, Y.; James, R. D.; Jalan, B. Self-Assembled Periodic Nanostructures Using Martensitic Phase Transformations. *Nano Lett.* **2021**, *21*, 1246−1252.
(45) Truttmann, T. K.; Liu, F.; Garcia-Barriocanal, J.; James, R. D.; Jalan, B. Strain Relaxation via Phase Transformation in High-Mobility $SrSnO_3$ Films. *ACS Appl. Electron. Mater.* **2021**, *3*, 1127−1132.
(46) Li, K.; Gao, Q.; Zhao, L.; Liu, Q. Transparent and conductive Sm-doped $SrSnO_3$ epitaxial films. *Opt. Mater.* **2020**, *107*, No. 110139.
(47) Liu, H.-R.; Yang, J.-H.; Xiang, H. J.; Gong, X. G.; Wei, S.-H. Origin of the superior conductivity of perovskite $Ba(Sr)SnO_3$. *Appl. Phys. Lett.* **2013**, *102*, No. 112109.
(48) Li, K.; Gao, Q.; Zhao, L.; Liu, Q. Electrical and Optical Properties of Nb-doped $SrSnO_3$ Epitaxial Films Deposited by Pulsed Laser Deposition. *Nanoscale Res. Lett.* **2020**, *15*, No. 164.
(49) Liu, Q. Z.; Wang, H. F.; Chen, F.; Wu, W. Single-crystalline transparent and conductive oxide films with the perovskite structure: Sb-doped $SrSnO_3$. *J. Appl. Phys.* **2008**, *103*, No. 093709.
(50) Gao, Q.; Li, K.; Zhao, L.; Zhang, K.; Li, H.; Zhang, J.; Liu, Q. Wide-Range Band-Gap Tuning and High Electrical Conductivity in La- and Pb-Doped $SrSnO_3$ Epitaxial Films. *ACS Appl. Mater. Interfaces* **2019**, *11*, 25605−25612.
(51) Kim, Y. M.; Park, C.; Ha, T.; Kim, U.; Kim, N.; Shin, J.; Kim, Y.; Yu, J.; Kim, J. H.; Char, K. High-k perovskite gate oxide $BaHfO_3$. *APL Mater.* **2017**, *5*, No. 016104.
(52) Maekawa, T.; Kurosaki, K.; Yamanaka, S. Thermal and mechanical properties of perovskite-type barium hafnate. *J. Alloys Compd.* **2006**, *407*, 44−48.
(53) Niu, F.; Meier, A. L.; Wessels, B. W. Epitaxial growth and strain relaxation of MgO thin films on Si grown by molecular beam epitaxy. *J. Vac. Sci. Technol., B: Microelectron. Nanometer Struct.* **2006**, *24*, No. 2586.
(54) Rossel, C.; Sousa, M.; Marchiori, C.; Fompeyrine, J.; Webb, D.; Caimi, D.; Mereu, B.; Ispas, A.; Locquet, J. P.; Siegwart, H.; Germann, R.; Tapponnier, A.; Babich, K. $SrHfO_3$ as gate dielectric for future CMOS technology. *Microelectron. Eng.* **2007**, *84*, 1869−1873.
(55) Acharya, M.; Banyas, E.; Ramesh, M.; Jiang, Y.; Fernandez, A.; Dasgupta, A.; Ling, H.; Hanrahan, B.; Persson, K.; Neaton, J. B.; Martin, L. W. Exploring the $Pb_{1-x}Sr_xHfO_3$ System and Potential for High Capacitive Energy Storage Density and Efficiency. *Adv. Mater.* **2022**, *34*, No. 2105967.
(56) Glazer, A. M. The classification of tilted octahedra in perovskite. *Acta Crystallogr., Sect. B: Struct. Crystallogr. Cryst. Chem.* **1972**, *28*, 3384−3392.
(57) Ye, C.; Pan, S. S.; Teng, X. M.; Li, G. H. Optical properties of $MgO-TiO_2$ amorphous composite films. *J. Appl. Phys.* **2007**, *102*, No. 013520.
(58) Bouhemadou, A.; Djabi, F.; Khenata, R. First principles study of structural, elastic, electronic and optical properties of the cubic perovskite $BaHfO_3$. *Phys. Lett. A* **2008**, *372*, 4527−4531.
(59) Feng, L.-p.; Liu, Z.-t.; Liu, Q.-j.; Tian, H. First-principles study of electronic and optical properties of *Pbnm* orthorhombic $SrHfO_3$. *Comput. Mater. Sci.* **2010**, *50*, 454−458.
(60) Schumann, T.; Raghavan, S.; Ahadi, K.; Kim, H.; Stemmer, S. Structure and optical band gaps of $(Ba,Sr)SnO_3$ films grown by molecular beam epitaxy. *J. Vac. Sci. Technol., A* **2016**, *34*, No. 050601.
(61) Zhang, W. F.; Tang, J.; Ye, J. Photoluminescence and photocatalytic properties of $SrSnO_3$ perovskite. *Chem. Phys. Lett.* **2006**, *418*, 174−178.
(62) Moreira, E.; Henriques, J. M.; Azevedo, D. L.; Caetano, E. W. S.; Freire, V. N.; Albuquerque, E. L. Structural, optoelectronic, infrared and Raman spectra of orthorhombic $SrSnO_3$ from DFT calculations. *J. Solid State Chem.* **2011**, *184*, 921−928.
(63) Haacke, G. New figure of merit for transparent conductors. *J. Appl. Phys.* **1976**, *47*, 4086−4089.

https://doi.org/10.1021/acsaelm.2c00581
ACS Appl. Electron. Mater. 2022, 4, 3623−3631